IEEE Photonics Journal
An IEEE Photonics Society Publication

Open Access

Liquid-Filled Hollow Core Bragg Fiber Sensors Using Different Bandgaps for High-Refractive-Index Sensing

Volume 11, Number 4, August 2019

Liang Shang, *Member, IEEE*
Sujuan Feng

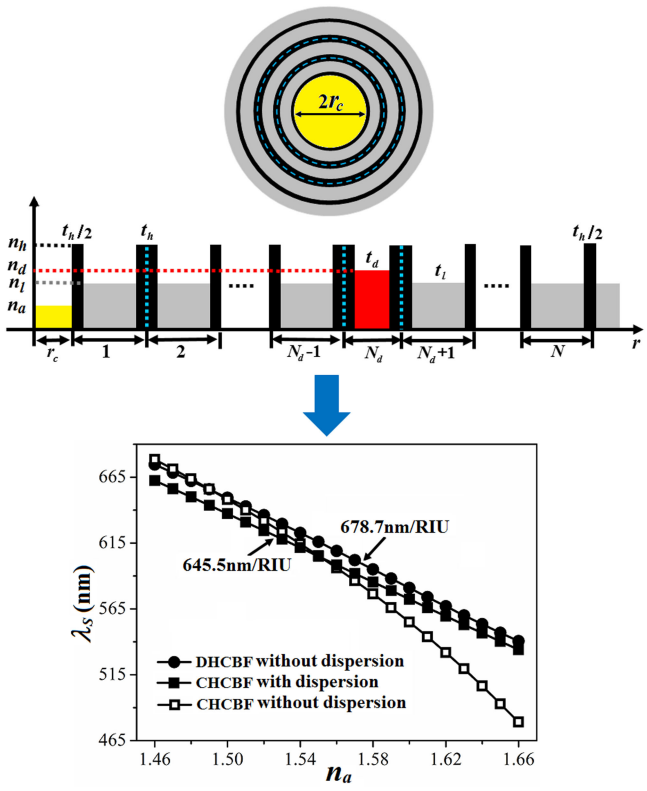

DOI: 10.1109/JPHOT.2019.2928601

Liquid-Filled Hollow Core Bragg Fiber Sensors Using Different Bandgaps for High-Refractive-Index Sensing

Liang Shang, *Member, IEEE*, and Sujuan Feng

School of Physics and Engineering, Shandong Provincial Key Laboratory of Laser Polarization and Information Technology, Qufu Normal University, Qufu 273165, China

DOI:10.1109/JPHOT.2019.2928601

Manuscript received March 12, 2019; revised June 24, 2019; accepted July 10, 2019. Date of publication July 15, 2019; date of current version July 24, 2019. This work was supported in part by the National Natural Science Foundation of China under Grants 11404185 and 11604343. Corresponding author: Liang Shang (email: shliang_sd@126.com.)

Abstract: Liquid-filled hollow core Bragg fibers (HCBFs) provide an excellent platform for refractive index (RI) sensing. The capacity for high-RI sensing based on higher order bandgaps of an HCBF is explored for higher sensitivity. We numerically compare the performances of an As_2S_3/PEI-based HCBF RI sensor using first-order and second-order photonic bandgaps (PBGs) for high-RI sensing. The influences of material dispersion and structural parameters on the sensing performance for both PBGs are investigated comparatively. Similar to the first-order PBG, the modification of the bandgap structure induced by material dispersion can also help to improve the linearity of an RI sensor using the second-order PBG of a conventional HCBF. For first-order and second-order PBGs including material dispersion, both a reduction in confinement loss and an improvement in sensitivity can be achieved by increasing the cladding period. In contrast, the influence of the period number on the sensitivity for a first-order PBG is contrary to that for a second-order PBG, which may be attributed to their different reflection characteristics. Furthermore, the comparative results show that a liquid-filled defect HCBF RI sensor using the second-order PBG can achieve high sensitivity and high linearity by optimizing the structural parameters of the defect layer. The proposed RI sensor would have great potential in the real-time measurement of high-RI liquid analytes.

Index Terms: Hollow core Bragg fibers, refractive index sensor, higher-order photonic bandgap.

1. Introduction

Refractive index (RI) sensors using microstructured optical fibers (MOFs) have attracted significant interest in the last two decades, owing to their great potential for biochemical sensing [1], [2]. The shift of the transmission spectrum with the RI of a liquid analyte filled in the air core or cladding of an MOF can be exploited as the sensing mechanism for RI measurements [3], [4]. In such an RI sensor, neither an elaborate preparation of microstructured devices [5], [6] nor an intricate coating of metal films on the surface of air holes [7], [8] is needed; hence, the fabrication difficulty is greatly reduced. However, the filling of a liquid analyte into holey MOFs (e.g., photonic crystal fibers) is time-consuming, severely restricting the response speed in real-time RI sensing. The advent of hollow core Bragg fibers (HCBFs) might bring about an opportunity for overcoming this issue.

As a distinct class of MOFs, HCBFs can effectively guide light in the air core using one-dimensional photonic bandgap (PBG) effect [9]. A typical HCBF generally has a large core with a

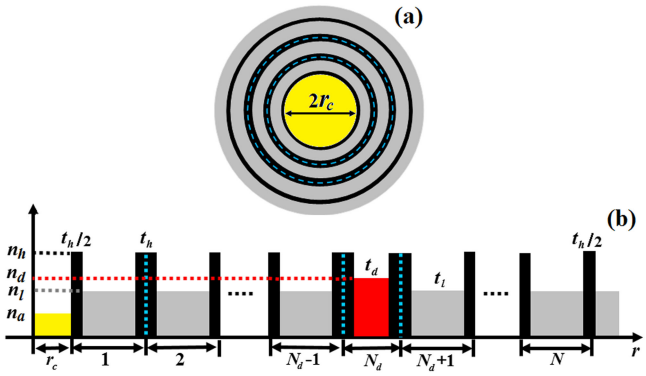

Fig. 1. (a) Schematic cross-section of a CHCBF; (b) radial refractive index profile of a DHCBF. The core and defect layer are marked in yellow and red, respectively. The dashed blue lines in (a) and (b) indicate ternary unit cells.

diameter of hundreds of micrometers and a multilayered cladding formed by high- or low-RI-contrast dielectric layers [10], [11]. The simple cladding construction of an HCBF would readily enable regulating the PBG structure and modal characteristics. In particular, HCBFs have advantages in filling the targeted liquid analyte into the air core over holey MOFs because their solid claddings can avoid a sophisticated selective filling pretreatment [12]. Thus, conventional HCBFs (CHCBFs) have been employed for RI sensing in recent years [13]–[16] by using the relationship between the central wavelength of the PBG and the RI of the liquid analyte in the core. A liquid-filled CHCBF sensor with a low-RI-contrast cladding generally has a much higher sensitivity but a narrower dynamic range than that with a high-RI-contrast cladding [13], [14]. For the simultaneous capacity of high sensitivity and large dynamic range, we previously proposed a high-linearity RI sensor using a liquid-filled defect HCBF (DHCBF) with a low-RI-contrast cladding [17], in which the characteristic wavelength was the resonance wavelength induced by the transverse coupling effect rather than the central wavelength of the bandgap in the CHCBF. However, the upper limit of the dynamic range for such an RI sensor is lower than 1.45. Thus, it cannot meet the requirement of applications in chemical industry or environmental monitoring, in which highly-sensitive and real-time RI measurements of high-RI liquid analytes (such as benzene, toluene and carbon disulfide [18]) are in great request [19].

As demonstrated in [13], the liquid-filled CHCBF with a high-RI-contrast cladding based on the combination of As_2S_3 and polyetherimide (PEI) is more suitable for high-RI sensing. The fundamental PBG of a high-RI-contrast-based CHCBF is generally large enough for broadband transmission. For a wider transmission band and a lower transmission loss, higher-order bandgaps in this kind of HCBF have also been exploited [20], [21]. However, to the best of our knowledge, the performance of a liquid-filled HCBF (CHCBF or DHCBF) RI sensor using higher-order PBGs has not been demonstrated in the literature. In this paper, we are motivated to explore the capacity for high-RI sensing based on the higher-order bandgap of a liquid-filled HCBF. The sensing performances of a liquid-filled HCBF RI sensor based on first-order and second-order PBGs are compared thoroughly. The results show that the second-order PBG is more beneficial for high sensitivity than the first-order PBG, which is essentially attributed to the difference in reflection characteristics of the multilayered cladding between them. Further, we believe that a liquid-filled DHCBF RI sensor using the second-order PBG would show great potential in applications of real-time high-RI measurement.

2. Structural Model and Simulation Method

2.1 Structural Model

Fig. 1(a) shows a schematic cross-section of a CHCBF. An air core with radius of r_c is filled with liquid analyte with an RI of n_a. A multilayered cladding consists of concentrically alternating dielectric

layers with high and low RIs (denoted by n_h and n_l, respectively). The high-RI layers with a thickness of t_h are marked in black, and the low-RI layers with a thickness of t_l are marked in gray. Note that the thicknesses of the innermost and outermost high-RI layers are $t_h/2$ to eliminate surface modes [22]. Accordingly, the ternary photonic crystal model is suitable for describing a multilayered cladding [23], in which each unit cell with a thickness of $\Lambda = t_h + t_l$ consists of a low-RI layer sandwiched by two high-RI layers. The outermost thick layer with the same RI as n_l indicates the protective cladding. In contrast, as illustrated in Fig. 1(b), the DHCBF can be regarded as a CHCBF with a low-RI layer in the N_d th period replaced by a so-called defect layer with a thickness of t_d and an RI of n_d. As a result of the transverse resonant coupling effect between the core modes and defect modes, the DHCBF acts as a band-rejection filter [24]. Accordingly, the resonance wavelength could be used as the characteristic wavelength for RI sensing in our previous work [17].

The material combination for the HCBFs employed in the following simulations is As_2S_3 and PEI, in accordance with the materials of an experimental work [13]. According to the material dispersion curves shown in [13], the RIs of As_2S_3 and PEI over the wavelength range of 400 nm to 900 nm can be expressed by, respectively,

$$n_h = A_8\lambda^8 + A_7\lambda^7 + A_6\lambda^6 + A_5\lambda^5 + A_4\lambda^4 + A_3\lambda^3 + A_2\lambda^2 + A_1\lambda + A_0 \tag{1}$$

$$n_l = B_8\lambda^8 + B_7\lambda^7 + B_6\lambda^6 + B_5\lambda^5 + B_4\lambda^4 + B_3\lambda^3 + B_2\lambda^2 + B_1\lambda + B_0 \tag{2}$$

where $A_8 = 2083.7544$, $A_7 = -9638.4722$, $A_6 = 18233.3688$, $A_5 = -17597.1956$, $A_4 = 8304.7053$, $A_3 = -725.5679$, $A_2 = -1045.7921$, $A_1 = 439.5335$, and $A_0 = -51.7423$; $B_8 = 1268.156$, $B_7 = -7040.1814$, $B_6 = 16950.1953$, $B_5 = -23102.3366$, $B_4 = 19482.7355$, $B_3 = -10403.9629$, $B_2 = 3434.8798$, $B_1 = -641.547$ and $B_0 = 53.7394$. In (1) and (2), λ is in units of micrometers. When material dispersions are not considered, the values of n_h and n_l are 2.582 and 1.685, respectively. In addition, the same structural parameters of the HCBFs as those in the experimental work [13] are listed as follows: $r_c = 165$ μm, $t_h = 0.38\Lambda$ and $t_l = 0.62$ Λ.

2.2 Simulation Method

The bandgap structure of a large-core HCBF can be approximately represented by that of a planar Bragg stack with the same parameters [9]. According to the Bloch-Floquet theorem, the band edges for transverse electric (TE) waves can be determined by

$$\left|\cos k_{xh}t_h \cos k_{xl}t_l - \frac{1}{2}\left(\frac{k_{xh}}{k_{xl}} + \frac{k_{xl}}{k_{xh}}\right)\sin k_{xh}t_h \sin k_{xl}t_l\right| = 1, \tag{3}$$

and the band edges for transverse magnetic (TM) waves can be determined by

$$\left|\cos k_{xh}t_h \cos k_{xl}t_l - \frac{1}{2}\left(\frac{n_l^2 k_{xh}}{n_h^2 k_{xl}} + \frac{n_h^2 k_{xl}}{n_l^2 k_{xh}}\right)\sin k_{xh}t_h \sin k_{xl}t_l\right| = 1. \tag{4}$$

In (3) and (4), $k_{xq} = \sqrt{[(\omega/c)n_q]^2 - \beta^2}$ is the transverse propagation constant, where β is the axial propagation constant, and q denotes h or l.

The bandgap structure of a planar Bragg stack can also be calculated by the transfer matrix method (TMM) [25]. As illustrated in Fig. 1(a), the multilayered cladding of a CHCBF is formed by N ternary unit cells. The characteristic matrix M_j for the jth unit cell is given by

$$M_j = \begin{bmatrix} \cos\delta_h & -\frac{i}{\eta_h}\sin\delta_h \\ -i\eta_h \sin\delta_h & \cos\delta_h \end{bmatrix} \begin{bmatrix} \cos\delta_l & -\frac{i}{\eta_l}\sin\delta_l \\ -i\eta_l \sin\delta_l & \cos\delta_l \end{bmatrix} \begin{bmatrix} \cos\delta_h & -\frac{i}{\eta_h}\sin\delta_h \\ -i\eta_h \sin\delta_h & \cos\delta_h \end{bmatrix} \tag{5}$$

where $\delta_h = \pi n_h t_h \cos\theta_h/\lambda$ and $\delta_l = 2\pi n_l t_l \cos\theta_l/\lambda$. $\eta_q = n_q \cos\theta_q$ and $\eta_q = n_q/\cos\theta_q$ are for the TE and TM waves, respectively, where q denotes h or l. θ_h and θ_l represent the incidence angles in the high- and low-index layers, respectively. λ is the wavelength in vacuum. Similarly, the characteristic

matrix M_{N_d} for the N_d th unit cell in a DHCBF is given by

$$M_{N_d} = \begin{bmatrix} \cos\delta_h & -\frac{i}{\eta_h}\sin\delta_h \\ -i\eta_h \sin\delta_h & \cos\delta_h \end{bmatrix} \begin{bmatrix} \cos\delta_d & -\frac{i}{\eta_d}\sin\delta_d \\ -i\eta_d \sin\delta_d & \cos\delta_d \end{bmatrix} \begin{bmatrix} \cos\delta_h & -\frac{i}{\eta_h}\sin\delta_h \\ -i\eta_h \sin\delta_h & \cos\delta_h \end{bmatrix} \tag{6}$$

where $\delta_d = 2\pi n_d t_d \cos\theta_d/\lambda$. $\eta_d = n_d \cos\theta_d$ and $\eta_d = n_d/\cos\theta_d$ are for the TE and TM waves, respectively. θ_d represents the incidence angle in the defect layer.

The total characteristic matrix M for the multilayered cladding of the CHCBF can be written as

$$M = \prod_{j=1}^{N} M_j. \tag{7}$$

In contrast, the total characteristic matrix for the multilayered cladding of the DHCBF can be written as

$$M = \left(\prod_{j=1}^{N_d-1} M_j\right) M_{N_d} \left(\prod_{j=N_d+1}^{N} M_j\right). \tag{8}$$

Given that the incidence angle in the fiber core is denoted by θ_{in}, the reflectivity $R_{s,p}(\theta_{in})$ from the multilayered cladding can be expressed as

$$R_{s,p}(\theta_{in}) = \left|\frac{(m_{11} + \eta_{out}m_{12})\eta_{core} - (m_{21} + \eta_{out}m_{22})}{(m_{11} + \eta_{out}m_{12})\eta_{core} + (m_{21} + \eta_{out}m_{22})}\right|^2 \tag{9}$$

where s and p represent the TE and TM waves, respectively. m_{11}, m_{12}, m_{21}, and m_{22} are the elements of M from (7) or (8). $\eta_{core} = n_a \cos\theta_{in}$ and $\eta_{out} = n_l \cos\theta_{out}$ are for the TE waves, and $\eta_{core} = n_a/\cos\theta_{in}$ and $\eta_{out} = n_l/\cos\theta_{out}$ are for the TM waves, where θ_{out} is the refraction angle in the outermost layer. The reflectivity as a function of wavelength at a given value of θ_{in} can be calculated from (9). Accordingly, the PBG can be denoted by the wavelength range with a reflectivity not less than 99% [23]. Compared with the Bloch-Floquet theorem, the TMM is more suitable for calculating the band structure of a multilayered cladding including material dispersion.

The confinement loss (CL) of a large-core CHCBF or DHCBF can be calculated by the ray optics method (ROM), which shows advantages of higher computation speed and reduced memory consumption over the finite element method (FEM) [26]. Based on the reflectivity calculated from (9), the CL can be determined by

$$CL = 4.34\frac{1 - R(\theta_c)}{2r_c \tan(\theta_c)} \ (\text{dB/m}) \tag{10}$$

with a characterized incidence angle of $\theta_c = \cos^{-1}(\lambda U_{mn}/(2\pi r_c n_a))$, and U_{mn} is the nth root of an (m-1)-order Bessel function. For pure TE and TM modes with $m = 0$, $R(\theta_c) = R_s(\theta_c)$ and $R(\theta_c) = R_p(\theta_c)$, respectively. For hybrid modes with $m \neq 0$, $R(\theta_c) = [R_s(\theta_c) + R_p(\theta_c)]/2$. Notably, here we concentrate our attention on the CL of HCBFs, in which case the absorption influences of both the liquid analyte and cladding materials are negligible.

3. Results and Discussion

The transmission band of a large-core HCBF (CHCBF or DHCBF) used for RI sensing mainly depends on the PBG for TM waves at glancing incidence [23]. Fig. 2 shows the band diagram of a one-dimensional photonic crystal (1DPC) with $n_h = 2.582$ and $n_l = 1.685$ for TM waves. The two solid lines of different colors represent the light lines ($\omega = \beta c/n_a$) for different values of n_a. The white regions above the light lines indicate PBGs of different orders. The first-, second- and third-order PBGs are distributed from the bottom up. In the case of a hollow core ($n_a = 1$), the transmission band for each PBG is determined by the frequency range between the intersection points of the light line (blue) with the band edges. In general, the PBG width can be estimated by the normalized bandwidth of $\Delta\omega_n = 2(\omega_H - \omega_L)/(\omega_H + \omega_L)$, where ω_H and ω_L are the frequencies

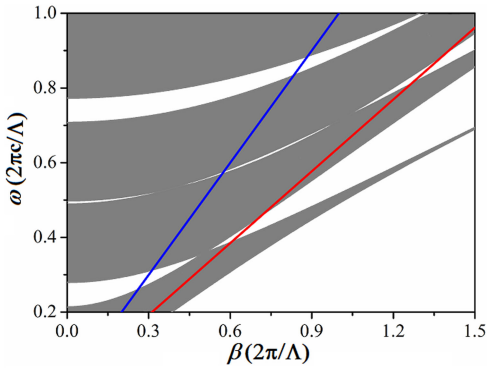

Fig. 2. Band diagram of a 1DPC for TM waves. The blue and red lines represent the light lines for $n_a = 1$ and $n_a = 1.56$, respectively. The white regions above the light lines indicate the PBGs of different orders.

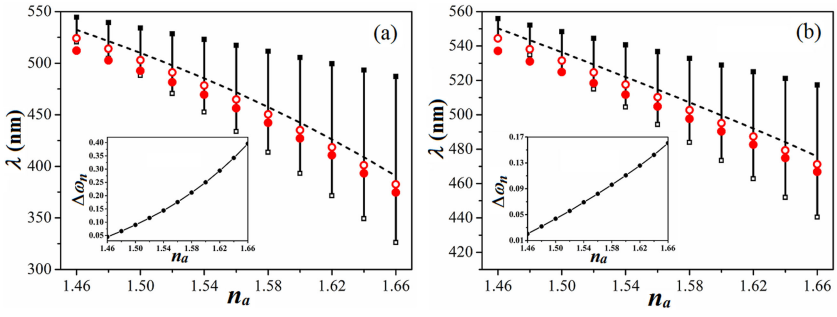

Fig. 3. Variation in the first-order PBG for TM waves with n_a in the cases of (a) excluding and (b) including material dispersion. In both (a) and (b), the dashed lines indicate λ_c as a function of n_a, and the insets show $\Delta\omega_n$ as a function of n_a. The solid and open circles represent λ_s for $N = 9$ and $N = 18$, respectively.

at the upper and lower edges, respectively. When a liquid analyte with $n_a > 1$ is filled into the air core, the light line will shift to the right, such as the red line for $n_a = 1.56$. It is well known that the Brewster phenomenon results in PBG collapses at certain frequencies (as shown in Fig. 2), and the effective index at the Brewster angle is given by $n_B = n_h n_l / \sqrt{n_h^2 + n_l^2}$ [27]. In a large-core HCBF, when the RI of liquid analytes gets close to n_B, no modes can be effectively guided in the core, so that the characteristics wavelength cannot be achieved from the transmission spectrum. Thus, for a continuous measurement without the disturbance of the Brewster phenomenon, it is better to enable n_B to be outside of the RI range. Fortunately, the lower limit of our targeted RI range (1.46 to 1.66) is still higher than n_B (1.411). Moreover, it is noted that the transmission spectrum for the second-order PBG is narrower than that for the first-order PBG, which helps to achieve a higher figure of merit (FOM) in RI sensing [28]. Considering the superiority of the TMM over the Bloch-Floquet theorem in calculations including material dispersion, in the following sections, we will compare the sensing performance of sensors based on different bandgaps using the TMM. The PBG at glancing incidence can be determined by the reflectivity spectrum at $\theta_{in} = 89^\circ$ [25].

3.1 Sensing Performance Based on the First-Order PBG

Fig. 3(a) shows the first-order PBG for TM waves as a function of n_a in the case of excluding material dispersion and $\Lambda = 200$ nm. Compared with the shift for the long-wavelength edge (solid squares), the blueshift for the short-wavelength edge (open squares) with increasing n_a is sharper. As shown in the inset, the normalized PBG width $\Delta\omega_n = 2(\lambda_H - \lambda_L)/(\lambda_H + \lambda_L)$ increases with increasing n_a,

TABLE 1
Sensitivity and R^2 for Different Values of N

N	Sensitivity (nm/RIU)	R^2
9	351.39	0.99795
12	359.56	0.99826
18	367.18	0.99873
25	371.21	0.99909

where λ_H and λ_L are the wavelengths at the long- and short-wavelength edges, respectively. When material dispersion is considered, similar blueshifts for both the long- and short-wavelength edges with increasing n_a can be observed in Fig. 3(b). However, the PBG widths are reduced more than those without material dispersion at the same n_a.

The central wavelength of the PBG (denoted by λ_c) can be utilized in principle as the characteristic wavelength (denoted by λ_s) for CHCBF-based RI sensing [13]. Notably, λ_c is the wavelength corresponding to the central frequency of the PBG, which can be determined by $2\lambda_H\lambda_L/(\lambda_H+\lambda_L)$ rather than $(\lambda_H+\lambda_L)/2$. The variations in λ_c with n_a in both cases are illustrated in Fig. 3(a) and (b), respectively. When material dispersion is included, the linear correlation between λ_c and n_a is dramatically enhanced (the adjusted R-square value R^2 resulting from linear fitting is 0.99933), which is attributed to the so-called "straightened out" effect on the bandgap edges (especially, the short-wavelength edge) illustrated in [13].

In the practical application of RI sensing, however, λ_s is generally represented by the central wavelength of the transmission spectrum in a liquid-filled CHCBF (i.e., the wavelength corresponding to the minimum transmission loss within the PBG range). Considering that the Gaussian-like HE_{11} mode is the dominant core mode in HCBFs, here we estimate λ_s by examining the CL spectrum of the fundamental HE_{11} mode [14]. Fig. 3(a) shows λ_s as a function of n_a for $N=9$ and $N=18$ in the case of excluding material dispersion. Obviously, λ_s deviates from λ_c at the same value of n_a, and the differences between them decrease with increasing n_a for a given value of N. A similar relationship between λ_s and λ_c in the case of including material dispersion is shown in Fig. 3(b). Notably, the calculated λ_s values at $n_a=1.462$ and $n_a=1.578$ for $N=9$ are 533.5 nm and 498.4 nm, respectively, which are in good agreement with the measured values of 533 nm and 500 nm presented in [13]. By comparing the variations in λ_s with n_a shown in Fig. 3(a) and (b), we can confirm the capacity of material dispersion in improving the linearity of a liquid-filled CHCBF RI sensor. Furthermore, we can see that the difference between λ_s and λ_c for a given value of n_a can be reduced by increasing N, which would influence the sensitivity and linearity. With n_a ranging from 1.46 to 1.66, the sensitivities and R^2 for different values of N in the case of including material dispersion are summarized in Table 1. Both the sensitivity and R^2 increase with increasing N and can reach the maximum values for a sufficiently large N, at which point λ_s would be equal to λ_c.

The influences of N on the sensitivity and linearity essentially depend on the variation of λ_s with N. In particular, as shown in Fig. 3, λ_s is even outside the PBG range for small values of n_a and N. Fig. 4(a) shows the CL of the HE_{11} mode within the first-order PBG in a liquid-filled CHCBF with $\Lambda=200$ nm and $n_a=1.46$ for different values of N. Here, the material dispersion is not considered for simplicity, so λ_s is merely influenced by N. As we can see from this figure, the redshift of λ_s to λ_c with increasing N and λ_s is outside the PBG range for $N=9$ and $N=12$. To confirm the correctness of the results calculated by the ROM, the CL for $N=9$ calculated by the FEM is shown in the inset of Fig. 4(a), in good agreement with the former result. To provide insight into the dependence of λ_s on N, we analyze the reflection characteristic of TM waves from the multilayered cladding. Fig. 4(b) shows the reflectivity of TM waves as a function of wavelength at θ_z for different values of N. As N increases, the wavelength ranges with higher reflectivity decrease, and the reflectivity peak (corresponding to λ_s) shifts towards longer wavelengths. As shown in Fig. 2, the PBG width at glancing incidence for $n_a=1.46$ is extremely limited, because the value of n_a is very close to $n_B=1.411$ (for $n_h=2.582$ and $n_l=1.685$). For a multilayered cladding with fewer periods (such as

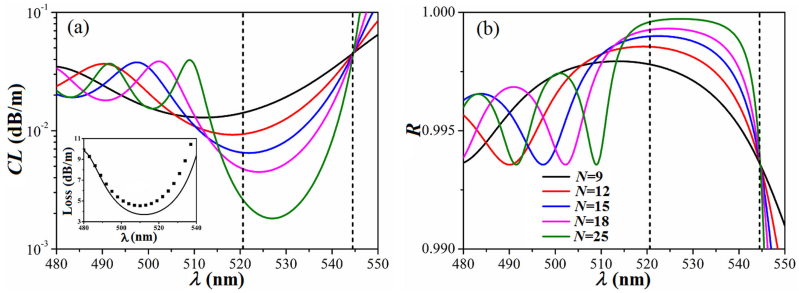

Fig. 4. (a) CL of the HE_{11} mode and (b) reflectivity for TM waves as a function of wavelength in a liquid-filled CHCBF with $\Lambda = 200$ nm and $n_a = 1.46$ for different values of N. The vertical dashed lines in both (a) and (b) indicate the PBGs at glancing incidence. The inset in (a) shows the CL for $N = 9$ calculated by the ROM (solid line) and FEM (solid squares).

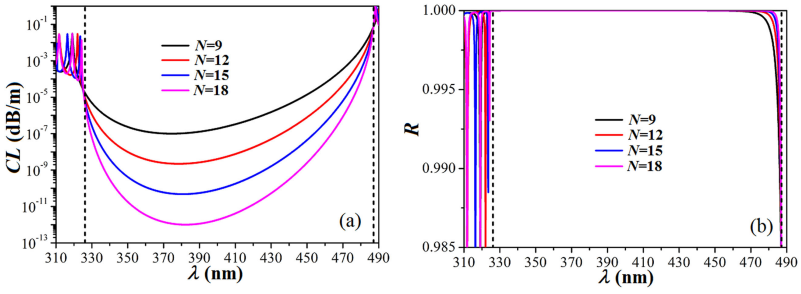

Fig. 5. (a) CL of the HE_{11} mode and (b) reflectivity as a function of wavelength in a liquid-filled CHCBF with $\Lambda = 200$ nm and $n_a = 1.66$ for different values of N. The vertical dashed lines in both (a) and (b) indicate the PBGs at glancing incidence.

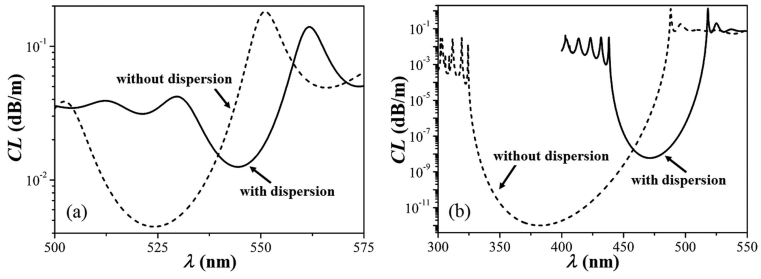

Fig. 6. Influence of material dispersion on the CL of the HE_{11} mode for (a) $n_a = 1.46$ and (b) $n_a = 1.66$, respectively.

$N = 9$), the coherent reflection within the narrow PBG is even weaker than the incoherent reflection outside the PBG [29], and the confinement of light in the core is not very tight despite the PBG effect. However, the coherent reflection is enhanced much more rapidly with increasing N than the incoherent reflection and gradually dominates in the reflectivity spectrum. As a result, the reflectivity within the PBG range is high enough to enable the reflectivity peak to occur for a large value of N.

As shown in Fig. 5(a), however, the influence of N on λ_s decreases for $n_a = 1.66$. Even for $N = 9$, λ_s is still within the PBG range. Compared with that for $n_a = 1.46$, the PBG for $n_a = 1.66$ is so wide that the coherent reflection is always stronger than the incoherent reflection illustrated in Fig. 5(b). This is the reason for the tight confinement of light in the core by a multilayered cladding even with fewer periods. In this case, increasing N can further enhance the coherent reflection within the PBG range, which would reduce both the transmission loss and the difference between λ_s and λ_c.

The transmission loss of a liquid-filled HCBF is also an important factor in practical RI sensing. Fig. 6(a) shows the influence of material dispersion on the CLs of the HE_{11} mode in a liquid-filled

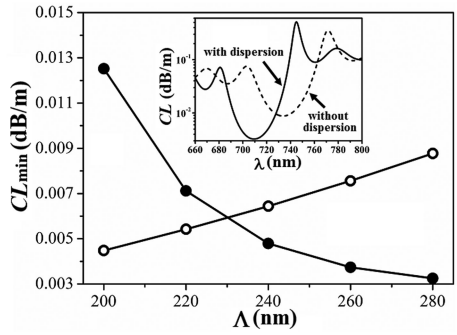

Fig. 7. $CL_{\min}$ as a function of Λ for $n_a = 1.46$ in the cases of including (solid circles) and excluding (open circles) material dispersion. The inset shows the loss spectra of the HE_{11} mode for $\Lambda = 280$ nm.

CHCBF with $\Lambda = 200$ nm and $N = 18$ for $n_a = 1.46$. When material dispersion is included, the increase in the CL is mainly attributed to the narrowing of the PBG (Fig. 3). A similar influence of material dispersion on the CL for $n_a = 1.66$ can be seen in Fig. 6(b). In this case, the CL with material dispersion included increases by approximately three orders of magnitude, but its absolute value is still very low due to the wide PBG for $n_a = 1.66$. Thus, we find that the influence is at an acceptable level. In contrast, the absolute CL for $n_a = 1.46$ is very large despite the small relative increase induced by material dispersion. Thus, it is necessary to reduce the CL by optimizing the structural parameters.

It is well known that the CL can be reduced by increasing N. Here, we focus on the influence of Λ on the CL. Fig. 7 shows the minimum CL (denoted by $CL_{\min}$) of the HE_{11} mode as a function of Λ for $n_a = 1.46$ at a given value of $N = 18$. It can be seen that $CL_{\min}$ increases with increasing Λ in the case of excluding material dispersion, while $CL_{\min}$ rapidly decreases with increasing Λ in the case of including material dispersion. When Λ is larger than 230 nm, $CL_{\min}$ with material dispersion included is lower than that with material dispersion excluded, and the difference between them increases with increasing Λ. For example, as seen from the inset of Fig. 7, $CL_{\min}$ with material dispersion included for $\Lambda = 280$ nm decreases by 62.9%, which is contrary to that shown in Fig. 6(a). The reduction in the CL essentially results from the wider PBG induced by material dispersion ($\Delta\omega_n$ increases from 0.0451 to 0.0548). Note that the variations in $CL_{\min}$ with Λ for $n_a = 1.66$ in both cases are similar to those for $n_a = 1.46$, except for the fact that $CL_{\min}$ with material dispersion included is always higher than that with material dispersion excluded. From the results mentioned above, we can conclude that material dispersion has two positive influences on the RI sensing performance of the liquid-filled As_2S_3/PEI-based CHCBF: improving the linearity of the RI sensor by using the "straightened out" effect and reducing the transmission loss by increasing Λ.

The increase in Λ can also improve the sensitivity in RI sensing by scaling up the PBG. In general, the operation wavelength for RI sensing is within the visible range [13], [14]. Because λ_s is longer than 700 nm for $\Lambda = 280$ nm (as shown in the inset of Fig. 7), we turn to the case of $\Lambda = 260$ nm, in which λ_c can cover the region of 556.8 nm to 674.1 nm for n_a ranging from 1.46 to 1.66. Compared with the value of approximately 371 nm/RIU for $\Lambda = 200$ nm shown in Fig. 3(b), the sensitivity of 589 nm/RIU with $R^2 = 0.99994$ increases by approximately 60%. Here, both the estimated sensitivities for comparison are based on linear fitting of λ_c and n_a, because the sensitivity can reach the maximum value at $\lambda_s = \lambda_c$.

3.2 Sensing Performance Based on the Second-Order PBG

Next, we examine the sensing performance of a liquid-filled CHCBF RI sensor based on the second-order PBG. To ensure that the second-order bandgap of the liquid-filled CHCBF is within the visible range, the period of Λ is set to 500 nm. Fig. 8(a) and (b) show the second-order PBGs for TM waves

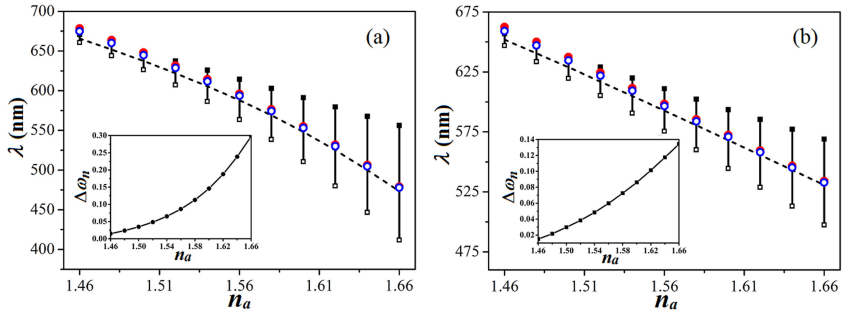

Fig. 8. Variation in the second-order PBG for TM waves with n_a in the cases of (a) excluding and (b) including material dispersion. In both (a) and (b), the dashed lines indicate λ_c as a function of n_a, and the insets show $\Delta\omega_n$ as a function of n_a. The solid and open circles represent λ_s for $N = 9$ and $N = 12$, respectively.

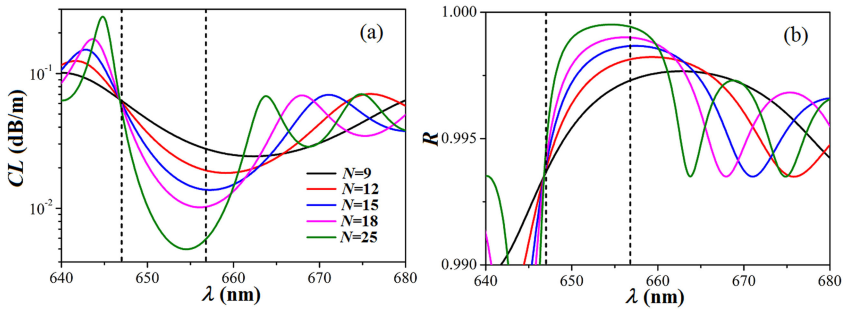

Fig. 9. (a) CL of the HE_{11} mode and (b) reflectivity for TM waves as a function of wavelength in a liquid-filled CHCBF with $\Lambda = 500$ nm and $n_a = 1.46$ for different values of N. The vertical dashed lines in both (a) and (b) indicate the PBGs at glancing incidence.

at different values of n_a in the cases of excluding and including material dispersion, respectively. In both cases, the variations in the second-order PBGs with n_a are very similar to those of the first-order PBGs. In particular, the "straightened out" effect on the second-order bandgap edges induced by material dispersion can still be observed. Consequently, the linear correlation between λ_c and n_a for the second-order PBG is dramatically improved. As shown in Fig. 8(b), the sensitivity resulting from linear fitting of λ_c and n_a is 607.26 nm/RIU with $R^2 = 0.99981$.

The variations in λ_s with n_a for $N = 9$ in both cases are also illustrated in Fig. 8(a) and (b). Similar to those shown in Fig. 3, it can be seen that λ_s differs from λ_c, and the difference decreases with increasing n_a. However, λ_s is longer than λ_c for the second-order PBG, which is in contrast to λ_s being shorter than λ_c for the first-order PBG. For a given value of n_a, the difference between λ_s and λ_c decreases with increased N up to 12. As a result of the influence of material dispersion, high linearity between λ_s and n_a can be seen in Fig. 8(b). The sensitivities for $N = 9$ and $N = 12$ are 645.47 nm/RIU with $R^2 = 0.99997$ and 634.77 nm/RIU with $R^2 = 0.99996$, respectively. As N increases, the sensitivity based on the second-order PBG decreases with a slightly reduced R^2 value; hence, it reaches the minimum value at $\lambda_s = \lambda_c$, which is contrary to that for the first-order PBG. According to the aforementioned results, the minimum sensitivity of 607.26 nm/RIU based on the second-order PBG for $\Lambda = 500$ nm is slightly higher than the maximum sensitivity of 589 nm/RIU based on the first-order PBG for $\Lambda = 260$ nm, which indicates the advantage of a second-order PBG over a first-order PBG for highly sensitive RI sensing.

As shown in Fig. 8(b), the enhancement in the sensitivity with a reduced N is attributed to the fact that the redshift of λ_s from λ_c increases with decreasing N, especially for small values of n_a. Fig. 9(a) shows the CL of the HE_{11} mode within the second-order PBG in a liquid-filled CHCBF with

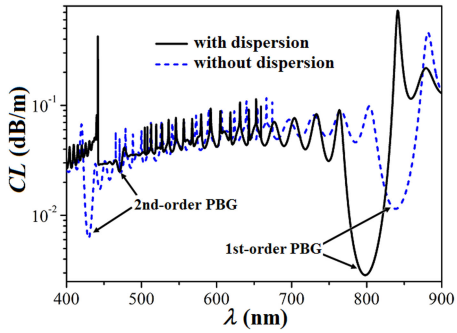

Fig. 10. Influence of material dispersion on the CL of the HE_{11} mode in a liquid-filled CHCBF with $\Lambda = 320$ nm, $N = 18$ and $n_a = 1.46$.

$n_a = 1.46$ for different values of N in the case of including material dispersion. As N decreases, λ_s shifts towards longer wavelengths, and even moves outside the long-wavelength bandgap edge. To understand the reason behind the dependence of λ_s on N, we plot the reflectivity spectra for TM waves at $\theta_z = 89.96^\circ$ in Fig. 9(b). The wavelength region with high reflectivity is in good agreement with the low-loss transmission window shown in Fig. 9(a). The emergence of λ_s outside the PBG for small values of N results from the weaker coherent reflection within the narrow PBG range than the incoherent reflection outside the PBG, which is seemingly similar to that for the first-order PBG illustrated in Fig. 4. However, λ_s for the second-order PBG is longer than the long-wavelength bandgap edge, while λ_s for the first-order PBG is shorter than the short-wavelength bandgap edge. The different behaviors of λ_s may be attributed to the different phase-shift variations between the first- and second-order PBGs [30]. As shown in Fig. 9, a much more rapid enhancement in the coherent reflection with increasing N for the second-order PBG gives rise to a shift of λ_s towards shorter wavelength rather than longer wavelength for the case of the first-order PBG.

Fig. 10 shows the difference in the loss spectrum of the HE_{11} mode between the first- and second-order PBGs in a liquid-filled CHCBF with $\Lambda = 320$ nm, $N = 18$, and $n_a = 1.46$. Here, Λ is set to 320 nm for both the first- and second-order PBGs covering the range of 400 nm to 900 nm. When the influence of material dispersion is excluded, the CL for the second-order PBG is lower than that for the first-order PBG, which is similar to the loss behavior of an all-silica-based Bragg fiber [20]. However, the former becomes approximately one order of magnitude higher than the latter in the case of including material dispersion. As discussed in [20], the CL depends on both the PBG width and the wavelength within the bandgap (i.e., the shorter wavelength for the second-order PBG corresponding to the lower CL). In the case of excluding material dispersion, the wavelength-dependence dominantly influences the CL, although the width is narrower for the second-order PBG than for the first-order PBG. In contrast, in the case of including material dispersion, the normalized width $\Delta\omega_n$ for the second-order PBG decreases from 0.0148 to 0.0013, while that for the first-order PBG increases from 0.0451 to 0.0625. The large width contrast between both PBGs induced by material dispersion would balance out the wavelength dependence to a great extent and correspondingly ensure a lower CL for the wider first-order PBG. Thus, we can further conclude that the influence of material dispersion on the CL is essentially attributed to its influence on the bandgap structure.

As shown in Fig. 10, the high loss for the second-order PBG in the liquid-filled As_2S_3/PEI-based CHCBF with $\Lambda = 320$ nm in the case of including material dispersion is not suitable for low-RI sensing (e.g., $n_a = 1.46$). According to the aforementioned results for the first-order PBG, when material dispersion is included, increasing Λ can not only reduce the CL, but it can also improve the sensitivity. In fact, similar influences of Λ on the CL and sensitivity are applicable for the second-order PBG. Fig. 11 shows CL_{min} as a function of n_a for $\Lambda = 500$ nm and $N = 9$ in the cases of including and excluding material dispersion. Here, N is set to 9 for the consistency with the parameter used in previous experimental work [13] and for higher sensitivity. It can be seen that

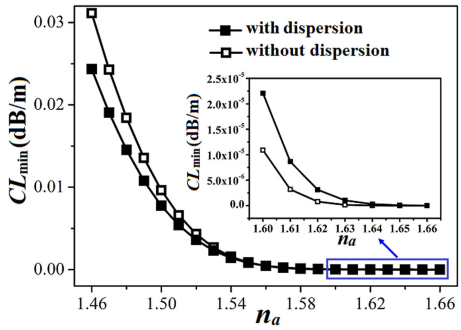

Fig. 11. CL_{min} as a function of n_a for $\Lambda = 500$ nm and $N = 9$ in the cases of including and excluding material dispersion. The inset shows the magnified region marked by the blue rectangle.

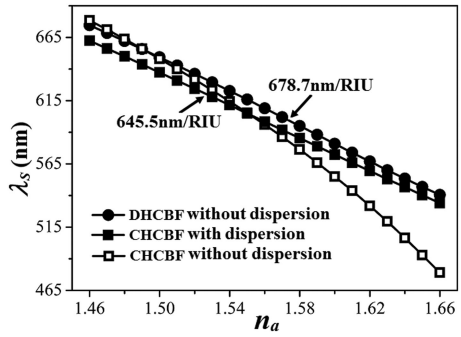

Fig. 12. Comparison of the sensing performance of liquid-filled CHCBF and DHCBF RI sensors using the second-order PBG.

CL_{min} for $n_a = 1.46$ with material dispersion included is lower than that without material dispersion. The values of CL_{min} in both cases decrease with increasing n_a. As shown in the inset of Fig. 11, however, CL_{min} with material dispersion included begins to exceed that without material dispersion when $n_a > 1.56$. The absolute CLs go down to the order of 10^{-4} dB/m for $n_a > 1.56$ (at least two orders of magnitude lower than those for $n_a = 1.46$) in the case of including material dispersion and hence are considered to fall to an acceptable level. The CL can be further reduced by increasing N, but this treatment would result in a lower sensitivity. Therefore, a tradeoff for N should be made between low CL and high sensitivity.

The linearity improvement of a liquid-filled CHCBF RI sensor based on the material combination of As_2S_3 and PEI essentially benefits from the influence of material dispersion on the bandgap structure for both the first-order and the second-order PBGs. However, this approach would be strongly restricted by the material dependence, because not all cladding materials (such as PMMA and PS in [14]) have the aforementioned "straightened out" effect on bandgap edges. In our previous work, a liquid-filled DHCBF was employed for a high-linearity RI sensor, in which the linearity could be improved by optimizing the RI, thickness and location of the defect layer [17]. The increased degrees of freedom can compensate for the influence of material dispersion and hence can provide more flexibility for improving the linearity. The relationship between λ_s and n_a for the second-order PBG in a liquid-filled DHCBF with $n_d = 2.582$, $t_d = 0.6t_h$, and $N_d = 2$ is illustrated in Fig. 12. Although the influence of material dispersion is excluded, a high value of $R^2 = 0.99973$ with a sensitivity of 678.7 nm/RIU can be achieved for n_a ranging from 1.46 to 1.66. We can see that such a sensitivity is even slightly higher than the value of 645.5 nm/RIU for a liquid-filled CHCBF RI sensor in the case of including the material dispersion. Moreover, compared with the wide transmission spectrum in the liquid-filled CHCBF, the narrow resonance spectrum in the liquid-filled DHCBF can help to achieve a higher FOM in RI sensing [17].

TABLE 2
Performance Comparison of the Typical Sensors for High-RI Measurement

Type of RI sensors	Sensitivity (nm/RIU)	Dynamic range	Ref.
Six-fold photonic quasi-crystal fiber based SPR sensor	4400	1.44-1.58	[19]
Multi-core holey fiber based SPR sensor	9231.3	1.43-1.53	[31]
Silver-coated hollow fiber based SPR sensor	2185-6607	1.509-1.763	[32]
Multi-core flat fiber based SPR sensor	23000	1.46-1.485	[33]
Silver-wire-filled hollow fiber based SPR sensor	4200-16200	1.47-1.51	[34]
Multilayer-coated capillary based SPR sensor	1951	1.5255-1.5781	[35]
Liquid-filled DHCBF sensor	678.7	1.46-1.66	(This)

The realization of a liquid-filled HCBF (CHCBF or DHCBF) RI sensor strongly depends on the fabrication of As_2S_3/PEI-based HCBFs. In practice, such HCBFs can be fabricated by using the preform-drawing technique demonstrated in [10]. Thus, this type of RI sensor is more cost-effective than surface plasmon resonance (SPR) sensors because of its simple metal-free construction and reduced fabrication difficulty. Nevertheless, it should be noted that the sensitivity of the liquid-filled HCBF RI sensor for high-RI measurement cannot be comparable to those of the SPR sensors [19], [31]–[35], as summerized in Table 2. Indeed, SPR is extremely sensitive to the RI variation of dielectric medium at the metal surface. Although a SPR sensor based on a liquid-filled HCBF for low-RI (around 1.32) measurement has been demonstrated in [7], the HCBF-based SPR sensor for high-RI measurement (especially, using higher-order bandgaps) yet to be investigated, is expected to be reported in our future work.

4. Conclusions

In this paper, we compared the performance of a liquid-filled As_2S_3/PEI-based HCBF RI sensor using first-order and second-order PBGs for high-RI sensing and analyzed the influencing factors. In particular, the capacity for high-RI sensing based on higher-order bandgaps has been demonstrated for the first time. Similar to the first-order PBG, the "straightened out" effect induced by material dispersion can also be used to improve the linearity of a liquid-filled CHCBF RI sensor based on the second-order PBG. In the case of including material dispersion, for both PBGs, increasing Λ can not only reduce the CL, but it can also improve the sensitivity. The influence of N on the sensitivity for the first-order PBG is contrary to that for the second-order PBG, which may be attributed to their different reflection characteristics. The comparative results show that a liquid-filled DHCBF RI sensor using the second-order PBG can be expected to achieve a higher sensitivity in high-RI sensing by optimizing the structural parameters. Although our proposed RI sensor possesses the advantages of large dynamic range, high linearity and simple metal-free construction in high-RI measurement, its sensitivity is still lower than those of the SPR sensors. In future, new sensing mechanisms, such as SPR, would be needed in liquid-filled HCBF RI sensors to further improve the sensitivity.

References

[1] D. K. C. Wu, B. T. Kuhlmey, and B. J. Eggleton, "Ultrasensitive photonic crystal fiber refractive index sensor," *Opt. Lett.*, vol. 34, no. 3, pp. 322–324, Feb. 2009.
[2] A. K. Paul, A. K. Sarkar, A. B. S. Rahman, and A. Khaleque, "Twin core photonic crystal fiber plasmonic refractive index sensor," *IEEE Sensors J.*, vol. 18, no. 14, pp. 5761–5769, Jul. 2018.

[3] J. Sun and C. C. Chan, "Photonic bandgap fiber for refractive index measurement," *Sens. Actuators B*, vol. 128, no. 1, pp. 46–50, Dec. 2007.
[4] B. Sun, M. Y. Chen, Y. K. Zhang, J. C. Yang, J. Q. Yao, and H. X. Cui, "Microstructured-core photonic-crystal fiber for ultra-sensitive refractive index sensing," *Opt. Exp.*, vol. 19, no. 5, pp. 4091–4100, Feb. 2011.
[5] X. Fang, C. R. Liao, and D. N. Wang, "Femtosecond laser fabricated fiber Bragg grating in microfiber for refractive index sensing," *Opt. Lett.*, vol. 35, no. 7, pp. 1007–1009, Apr. 2010.
[6] A. Khaleque *et al.*, "Integration of bow-tie plasmonic nano-antennas on tapered fibers," *Opt. Exp.*, vol. 25, no. 8, pp. 8986–8996, Apr. 2017.
[7] B. Gauvreau, A. Hassani, M. F. Fehri, A. Kabashin, and M. A. Skorobogatiy, "Photonic bandgap fiber-based surface plasmon resonance sensors," *Opt. Exp.*, vol. 15, no. 18, pp. 11413–11426, Sep. 2007.
[8] D. Li, W. Zhang, H. Liu, J. Hu, and G. Zhou, "High sensitivity refractive index sensor based on multicoating photonic crystal fiber with surface plasmon resonance at near-infrared wavelength," *IEEE Photon. J.*, vol. 9, no. 2, Apr. 2017, Art. no. 6801608.
[9] Y. Fink *et al.*, "A dielectric omnidirectional reflector," *Science*, vol. 282, pp. 1679–1682, Nov. 1998.
[10] K. Kuriki *et al.*, "Hollow multilayer photonic bandgap fibers for NIR applications," *Opt. Exp.*, vol. 12, no. 8, pp. 1510–1517, Apr. 2004.
[11] E. Pone *et al.*, "Drawing of the hollow all-polymer Bragg fibers," *Opt. Exp.*, vol. 14, no. 13, pp. 5838–5852, Jun. 2006.
[12] Y. Huang, Y. Xu, and A. Yariv, "Fabrication of functional microstructured optical fibers through a selective-filling technique," *Appl. Phys. Lett.*, vol. 85, no. 22, pp. 5182–5184, Nov. 2004.
[13] K. J. Rowland, S. V. Afshar, A. Stolyarov, Y. Fink, and T. M. Monro, "Bragg waveguides with low-index liquid cores," *Opt. Exp.*, vol. 20, no. 1, pp. 48–62, Jan. 2011.
[14] H. Qu and M. Skorobogatiy, "Liquid-core low-refractive-index-contrast Bragg fiber sensor," *Appl. Phys. Lett.*, vol. 98, no. 20, May 2011, Art. no. 201114.
[15] H. Qu and M. Skorobogatiy, "Resonant bio- and chemical sensors using low-refractive-index-contrast liquid-core Bragg fibers," *Sens. Actuators B*, vol. 161, no. 1, pp. 261–268, Jan. 2012.
[16] J. Li, H. Qu, and M. Skorobogatiy, "Simultaneous monitoring the real and imaginary parts of the analyte refractive index using liquid-core photonic bandgap Bragg fibers," *Opt. Exp.*, vol. 23, no. 18, pp. 22963–22976, Sep. 2015.
[17] K. Zheng and L. Shang, "High-linearity refractive index sensor based on analyte-filled defect hollow core Bragg fiber," *IEEE Photon. Technol. Lett.*, vol. 29, no. 16, pp. 1391–1394, Aug. 2017.
[18] S. Kedenburg, M. Vieweg, T. Gissibl, and H. Giessen, "Linear refractive index and absorption measurements of nonlinear optical liquids in the visible and near-infrared spectral region," *Opt. Mater. Express*, vol. 2, no. 11, pp. 1588–1611, Nov. 2012.
[19] S. Chu, K. Nakkeeran, A. M. Abobaker, S. S. Aphale, P. R. Babu, and K. Senthilnathan, "Design and analysis of surface-plasmon-resonance-based photonic quasi-crystal fiber biosensor for high-refractive-index liquid analytes," *IEEE J. Sel. Topics Quantum Electron.*, vol. 25, no. 2, Mar./Apr. 2019, Art. no. 6900309.
[20] K. J. Rowland, A. V. Shahraam, and T. M. Monro, "Novel low-loss bandgaps in all-silica Bragg fibers," *J. Lightw. Technol.*, vol. 26, no. 1, pp. 43–51, Jan. 2008.
[21] L. Shi, W. Zhang, J. Jin, Y. Huang, and J. Peng, "Multi-wavelength transmission of hollow-core Bragg fiber with modified binary one-dimensional photonic crystal cladding," *J. Lightw. Technol.*, vol. 30, no. 10, pp. 1492–1498, May 2012.
[22] O. Shapira *et al.*, "Surface emitting fiber lasers," *Opt. Exp.*, vol. 14, no. 9, pp. 3929–3935, May 2006.
[23] L. Shang, X. Yang, Y. Xia, and H. Wang, "Hollow core Bragg fibers with a heterostructured cladding based on ternary one-dimensional photonic crystal for mid-infrared broadband and low-loss transmission," *J. Lightw. Technol.*, vol. 32, no. 9, pp. 1717–1725, May 2014.
[24] G. Benoit, K. Kuriki, J. F. Viens, J. D. Joannopoulos, and Y. Fink, "Dynamic all-optical tuning of transverse resonant cavity modes in photonic bandgap fibers," *Opt. Lett.*, vol. 30, no. 13, pp. 1620–1622, Jul. 2005.
[25] S. K. Awasthi, U. Malaviya, and S. P. Ojha, "Enhancement of omnidirectional total-reflection wavelength range by using one-dimensional ternary photonic bandgap material," *J. Opt. Soc. Amer. B*, vol. 23, no. 12, pp. 2566–2571, Dec. 2006.
[26] L. Shang and K. Zheng, "Design of hollow core Bragg fibers for a compact fluorescence sensing scheme," *IEEE Photon. J.*, vol. 9, no. 2, Apr. 2017, Art. no. 7101515.
[27] Y. Zhang and I. D. Robertson, "Single-mode terahertz Bragg fiber design using a modal filtering approach," *IEEE Trans. Microw. Theory Tech.*, vol. 58, no. 7, pp. 1985–1992, Jul. 2010.
[28] D. J. J. Ju and H. P. Ho, "Recent advances in plasmonic photonic crystal fibers: Design, fabrication and applications," *Adv. Opt. Photon.*, vol. 9, no. 2, pp. 257–314, Jun. 2017.
[29] A. Argyros, "Guided modes and loss in Bragg fibers," *Opt. Exp.*, vol. 10, no. 24, pp. 1411–1417, Dec. 2002.
[30] K. S. Wu, J. W. Dong, and H. Z. Wang, "Phase engineering of one dimensional defective photonic crystal and applications," *Appl. Phys. B*, vol. 91, pp. 145–148, Apr. 2008.
[31] B. Shuai, L. Xia, Y. Zhang, and D. Liu, "A multi-core holey fiber based plasmonic sensor with large detection range and high linearity," *Opt. Exp.*, vol. 20, no. 6, pp. 5974–5986, Mar. 2012.
[32] B. H. Liu, Y. X. Jiang, X. S. Zhu, X. L. Tang, and Y. W. Shi, "Hollow fiber surface plasmon resonance sensor for the detection of liquid with high refractive index," *Opt. Exp.*, vol. 21, no. 26, pp. 32349–32357, Dec. 2013.
[33] A. A. Rifat, G. A. Mahdiraji, Y. M. Sua, R. Ahmed, Y. G. Shee, and F. R. M. Adikan, "Highly sensitive multi-core flat fiber surface plasmon resonance refractive index sensor," *Opt. Exp.*, vol. 24, no. 3, pp. 2485–2495, Jan. 2016.
[34] N. Luan and J. Yao, "High refractive index surface plasmon resonance sensor based on a silver wire filled hollow fiber," *IEEE Photon. J.*, vol. 8, no. 1, Feb. 2016, Art. no. 4800729.
[35] M. Lu *et al.*, "Dual channel multilayer-coated surface plasmon resonance sensor for dual refractive index range measurements," *Opt. Exp.*, vol. 25, no. 8, pp. 8563–8570, Apr. 2017.